PCCP

Accepted Manuscript

ROYAL SOCIETY OF CHEMISTRY

www.rsc.org/pccp

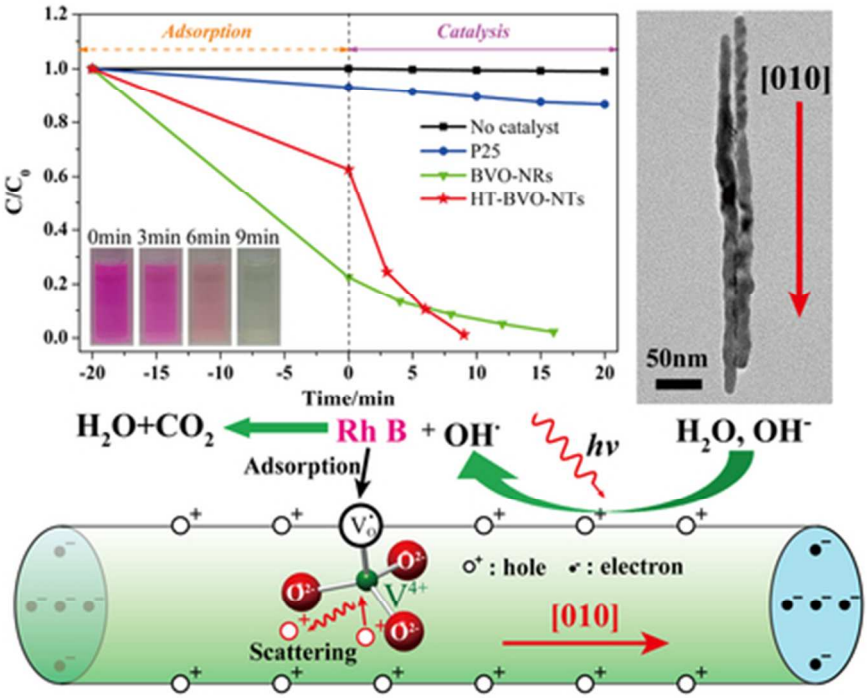

Self-doped, [010] oriented $BiVO_4$ nanorods with plentiful oxygen vacancies on the surface exhibit strong adsorbability and highly efficient photocatalytic activity.
38x30mm (300 x 300 DPI)

Journal Name

RSCPublishing

ARTICLE

Facile Synthesis of V^{4+} Self-doped, [010] Oriented $BiVO_4$ Nanorods with Highly Efficient Visible Light-induced Photocatalytic Activity

Cite this: DOI: 10.1039/x0xx00000x

Received 00th January 2012,
Accepted 00th January 2012

DOI: 10.1039/x0xx00000x

www.rsc.org/

Yangyang Zhang, Yiping Guo*, Huanan Duan, Hua Li, Chongyang Sun, Hezhou Liu*

Monodispersed monoclinic $BiVO_4$ nanorods grown along [010] direction were prepared using a one-step low temperature hydrothermal method in the presence of the low-cost, nontoxic sodium oleate served as chelating agent. The $BiVO_4$ nanorods with diameters of 15-20 nm possess a huge specific surface area as large as 28.2 m^2 g^{-1}, which can endow it with high photocatalytic activity and strong adsorption of reactants. Meanwhile, the specific [010] growth direction is capable of facilitating electron-hole separation efficiency by accumulating electrons on {010} facets. Thus, highly efficient photocatalytic activity of the as-prepared $BiVO_4$ nanorods under visible light, which far surpasses that of commercial P25, is demonstrated by degradation of rhodamine B and phenol. Plentiful V^{4+} species, which can bring oxygen vacancies, is detected implying the as-obtained nanorods are self-doped $BiVO_4$. Significantly, 61% of rhodamine B is adsorbed by the $BiVO_4$ nanorods before irradiation owing to the appearance of plentiful O^{2-} and OH^- species on the surface adsorbed by oxygen vacancies. More excitingly, the excellent visible-light-driven photocatalytic activity of the as-obtained $BiVO_4$ nanorods can be further elevated to an unprecedented level, roughly doubled, after applying a low temperature heat treatment process at 230 ℃ for 2 h and this improvement could primarily be ascribed to its optimized charge-carrier transport characteristics resulted from elevated crystallinity and decreased V^{4+} species.

Introduction

Photocatalytic oxidation of organic pollutants in waste water, especially that from the textile industry and the photographic industry, utilizing solar energy has been regarded as a very promising environmentally friendly way to remedy the gradually deteriorating water ecology. [1, 2] Driven by this idea, various kinds of photocatalysts have been developed up to now and among which titanium dioxide (TiO_2) is the most extensively investigated one owing to its favorable properties including relatively low cost, non-toxicity, high chemical- and photo- stability etc. [3-6] Unfortunately, it can merely take advantage of the ultraviolet light which accounts for less than 5% of the solar energy due to its relatively wide band gap of 3.2 eV (anatase), resulting in poor visible light photocatalytic performance.[5, 7, 8] Therefore, it is quite essential to develop a more efficient visible light responsive photocatalyst which inherits the advantages of TiO_2 while overcomes its shortcomings.

Among the narrow band gap semiconductors that have been studied previously, monoclinic bismuth vanadate (*m*-$BiVO_4$) stands out by combining the cost effective, eco-friendly and chemically stable virtues with a narrow band gap of about 2.4 eV, which endows it with excellent visible light absorption. [9-14] However, the photo-oxidation performance of pure *m*-$BiVO_4$ is not impressive as it suffers from excessive electron-hole recombination, [15] poor charge transfer property [16] and weak surface adsorption effects [17].

It is reported that not only TiO_2 but also *m*-$BiVO_4$ shows diverse photo-oxidation abilities on different facets indicating the distinguishing electron-hole separation process resulted by their various energy levels.[18-20] The well-designed experiment conducted by Li *et al.* demonstrated that electrons tended to accumulate on {010} faces while holes preferred transferring to {110} faces (with the cell choice in the *I2/a* space group) implying less exposed {010} facets in *m*-$BiVO_4$ are advantageous to its photo-oxidation reaction. [19] Thus, it is of great importance to prepare rod-like *m*-$BiVO_4$ grown along [010] direction.

Silversmit *et al.* demonstrated that V^{5+} could be easily reduced to V^{4+}, namely self-doping, and brought about oxygen vacancies. [21] Reduced $BiVO_4$ containing V^{4+} species has been obtained in several different ways, such as electrochemical reduction, hydrotreating and hydrothermal with reducing additives. [22-24] However, oxygen vacancy is a double-edged sword, because on one hand the oxygen vacancies are beneficial to the adsorption of reactants and can enhance electron-hole separation, but on the other hand, analogous to traditional doping, V^{4+} with larger radiuses can act as scattering centers and result in lattice distortion which subsequently reduce the effective diffusion length of holes. [10, 23] Hence, an excess of V^{4+} is detrimental to the photocatalytic performance of *m*-$BiVO_4$ and desired *m*-$BiVO_4$ with

both excellent absorbability and photocatalytic property can be achieved by adjusting the content of V^{4+} through a low temperature heat treatment. Nevertheless, it is still difficult to prepare *m*-$BiVO_4$ with abundant V^{4+} directly using hydrothermal method because many reducing additives will change the phases of the products.

Rod-like structures have been received more and more attention due to its large specific surface area and other unique properties. [25, 26] *m*-$BiVO_4$ nanorods with diameters ranging from 50 nm to 100 nm have been prepared in several different ways and their specific surface areas can be as large as 10 $m^2\ g^{-1}$ which is 13 times higher than that of bulk *m*-$BiVO_4$ (0.7 $m^2\ g^{-1}$). [1, 27, 28] However, their photocatalytic performances and adsorption efficiencies are still unimpressive possibly because the diameter is not small enough and the monodispersity is poor. Besides, growth directions of these nanorods remain unknown and their preparation needs either toxic organic additives or strong acids. Therefore, it is meaningful to develop a green route to fabricate monodispersed *m*-$BiVO_4$ nanorods with smaller diameter and specific growth direction.

Herein, we report a cost effective, green, one-step method to synthesize monodispersed *m*-$BiVO_4$ with a specific growth direction of [010] at a temperature as low as 100 ℃. The relatively high photocatalytic activity and adsorption ability of the obtained pure *m*-$BiVO_4$ nanorods are characterized by photodegradation of rhodamine B (Rh B) and phenol under visible light irradiation (λ>420 nm). In the present study, we also describe the effect of the concomitant V^{4+} species on the charge transport characteristics. By eliminating the excessive V^{4+} through a low temperature heat treatment, the photo-oxidation activity of the as-obtained *m*-$BiVO_4$ nanorods could be doubled in spite of its reduced adsorption ability. The main paragraph text follows directly on here.

Experimental

Synthesis of m-$BiVO_4$ nanorods

All chemicals used in this work were of analytical grade and used without further purification. In a typical synthesis procedure, 0.4 mmol $Bi(NO_3)_3\ 5H_2O$ was dissolved in 20 ml deionized (DI) water followed by adding 1.2 mmol sodium oleate under constant stirring for 2 h. 0.4 mmol NH_4VO_3 was dissolved in 20 ml DI water as well under vigorous stirring for 2 h. Afterwards, the above solutions were mixed together to form a stable salmon suspension with constant stirring for 1 h. The resulting suspension together with a magnetic stirrer were then transferred into a 50 ml Teflon-lined stainless steel autoclave to 80% of its total volume. The autoclave was held at 100 ℃ for 24 h and cooled down to room temperature naturally. After washing the black product with DI water and absolute ethanol for several times to remove any possible diffluent impurities and drying at 60 ℃ for 5 h, a vivid yellow powder named as BVO-NRs was obtained. Heat treatment was carried out in a furnace at 230 ℃ for 2 h with a heating rate of 5 ℃ min^{-1} and the resulting powder was denoted as HT-BVO-NRs hereafter.

Preparation of m-$BiVO_4$ nanorods film electrode

m-$BiVO_4$ nanorods film electrodes were prepared on indium tin oxide (ITO) conducting glass using electrophoretic deposition technique. 150 mg *m*-$BiVO_4$ nanorods (BVO-NRs or HT-BVO-NRs) along with 20 mg iodine were added into 75 ml acetone under sonication for 10 min to form a homogeneous suspension. The electrophoretic deposition was carried out employing ITO glasses as both work electrode and counter electrode at a bias of 200 V for 1 min and the distance between the electrodes was 8 cm.[29] After drying at 70 ℃ for 24 h, the obtained electrodes were connected with a strip of copper foil on the conductive side and then sealed using insulating epoxy resin to control the exposed area to be 1 cm×1 cm.

Characterization

Morphologies of BVO-NRs and HT-BVO-NRs were observed with a field emission transition electron microscope (JEM 2100F) with an acceleration voltage of 200 kV. The Brunauer-Emmett-Teller (BET) specific surface area was determined by nitrogen adsorption using an ASAP 2020 M (Micromeritics) specific surface area analyzer. Phase purity and crystal perfection were determined by powder X-ray diffraction (XRD) analysis (Rigaku D/MAX255ovl/84, Cu K_α radiation) from 10° to 70° (2θ) at a scan rate of 4 °/min under 35 kV and 200 mA. Fourier transform infrared (FT-IR) spectra were obtained on a Nicolet 6700 (ThermoFisher) Fourier transform infrared spectrometer using the KBr pellet technique in the range of 400-4000 cm^{-1}. The chemical states of elements were analyzed on an AXIS ULTRA DLD spectrometer (Kratos) working in the pass energy mode at 40 eV, and the Al K_α radiation was used as the excitation source. The binding energy reference was taken at 284.8 eV for the C 1s peak arising from surface hydrocarbons. The relative oxidation states of the V in these samples were further confirmed by electron paramagnetic resonance (EPR) measurements using a Bruker EMX-8/2.7 spectrometer operating at X-band frequency (9.88 GHz) and 2.02 mW. Diffuse-reflectance spectroscopy of the as prepared samples was measured using UV-Visible spectrometer (PerkinElmer 750S) between 300-900 nm with analytical $BaSO_4$ powder as the baseline correction material.

Photocatalytic activity and electrochemical impedance spectroscopy measurement

The photocatalytic activity was evaluated by photodegradation of Rh B and colorless phenol. Typically, 0.6 mmol *m*-$BiVO_4$ was added into 50 ml 10 mg L^{-1} Rh B aqueous solution or 100 ml 50mg L^{-1} phenol solution under sonication and stirring in dark for 1 h to reach adsorption-desorption equilibrium. The suspension was then irradiated by a 350 W xenon lamp equipped with a 420 nm light cut-off filter at 15 cm above the liquid level. At given time intervals, 2.5 ml suspension was collected and centrifuged at 10000 rpm for 5 min to remove the catalysts. The concentration of Rh B and phenol was determined by measuring the maximum absorbance at 554 nm and 269 nm, respectively, using the UV-Vis spectrometer.

The electrochemical impedance spectroscopy (EIS) of BVO-NRs and HT-BVO-NRs film electrodes were measured by an electrochemical workstation (RST) in a three electrode setup in 0.1 M $NaHCO_3$ (pH 7 phosphate buffer) electrolyte with platinum (Pt) electrode acting as the counter electrode and saturated calomel electrode (SCE) in saturated potassium chloride (KCl) as the reference electrode under a constant bias of 0.7 V (vs. SCE) with an AC amplitude of 10 mV from 100 KHz to 100 mHz. The working electrode was also irradiated using a 350 W xenon lamp equipped with a 420 nm light cut-off filter from the uncoated side of the ITO glass (back side).

Results and discussion

As shown in Fig. 1, monodispersed *m*-$BiVO_4$ nanorods were successfully prepared at a temperature as low as 100 ℃. Compared with previously reported route, this method is greener and more energy efficient, and the monodispersity of the products is better. [1, 28, 30] According to Fig. 1(a) and (b), the nanorods of BVO-NRs are 15-20 nm in diameter, 70-450 nm in

length and the aspect ratio can be as large as 30. It is found that these nanorods prefer gathering together in parallel to lower their surface energy indicating a large specific surface area which is measured to be 28.2 m^2 g^{-1}, nearly three times to the values of those nanorods reported previously.[1, 28, 30] Fig. 1(c) shows the HR-TEM (high-resolution TEM) image of a typical nanorod and its corresponding selected-area electron diffraction (SAED) is displayed in Fig. 1(d). The evident fringes observed in the HR-TEM image are basically vertical to the longitudinal direction of the nanorod and their spacing is calculated to be 0.291 nm which agrees well with the spacing of (040) lattice planes of *m*-$BiVO_4$ with a space group of *I2/a*. Hence, the *m*-$BiVO_4$ nanorods preferentially grow along [010] direction. The diffraction spots in the SAED pattern (indexed as $[10\bar{2}]$ zone) can be indexed as the (020), (211) and $(\bar{2}1\bar{1})$ reflections. It is worth noting that the SAED pattern is a little bit obscure and appears to be made up of two sets of overlapped diffraction spots, as shown in Fig. S1. This phenomenon can be ascribed to the instability of *m*-$BiVO_4$ nanorods under high-energy electron beam, as displayed in Fig. S2. The ordered atomic arrangement is readily destroyed and *m*-$BiVO_4$ quantum dots with dimension around 5 nm are generated after the electron beam focuses on the nanorod for about 5 seconds. This result may be of great importance for providing a novel approach to prepare ternary metal oxide quantum dots which are hard to synthesize, but it remains to be further investigated. The TEM image and SAED pattern of HT-BVO-NRs are shown in Fig. S3. Obviously, the morphology of the as-obtained *m*-$BiVO_4$ nanorods remains unchanged after heating at 230 ℃. Besides, the BET surface area of HT-BVO-NRs, which is determined to be 27.8 m^2 g^{-1}, is also very close to that of BVO-NRs.

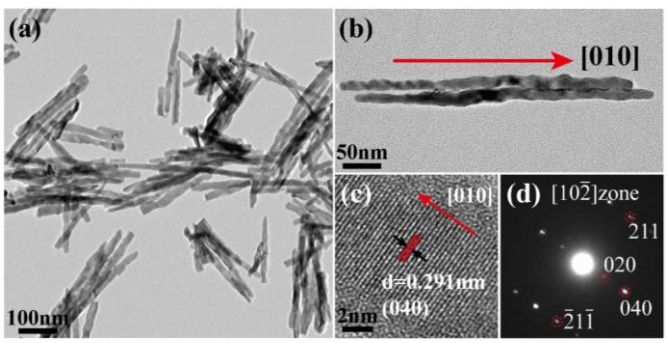

Fig.1 (a) A low-magnification TEM image, (b) a high-magnification TEM image, (c) a high-resolution TEM image and (d) the selected-area electron diffraction pattern for the as prepared BVO-NRs.

The phase, crystallinity and crystal perfection of the as-prepared BVO-NRs and HT-BVO-NRs are examined by XRD analysis and their indexed XRD patterns are shown in Fig. 2. All the peaks can be well assigned to the single-phase monoclinic scheelite *m*-$BiVO_4$ with a space group of *I2/a* (JCPDS card no. 14-0688). It is well known that the minor diffraction peak at 15.1 ° can be employed to distinguish *m*-$BiVO_4$ from tetragonal scheelite $BiVO_4$ (*t*-$BiVO_4$). Apparently, the small characteristic diffraction peak at 15.1 ° is observed for both samples implying their monoclinic feature. Of note, the $I_{max}/I_{15.1°}$ values (where I_{max} and $I_{15.1°}$ represent the intensities of the strongest peak at 29 ° and the peak at 15.1 ° in each pattern, respectively) of both BVO-NRs and HT-BVO-NRs are either close to or smaller than those of the standard cards, see Table S1, indicating no *t*-$BiVO_4$ exists in our samples. It can be seen from Fig. 2 that the intensities of the diffraction peaks of BVO-NRs are much weaker than those of HT-BVO-NRs, suggesting that the crystallinity of BVO-NRs is worse and could be notably improved *via* heat treatment. It is reasonable that there are much more defects in the bulk phase of the as-obtained BVO-NRs in comparison with HT-BVO-NRs.[31, 32] These defects could act as electron-hole recombination center and charge carrier scattering center which will impair the photocatalytic property seriously. Many previous studies have proved that high crystallinity is advantageous for photocatalytic activity and our following photocatalytic degradation results are consistent well with these former studies. [33-35] Magnified views of the peaks at around 35 ° of BVO-NRs and HT-BVO-NRs are compared in the inset of Fig. 2. After heat treatment, the broad protuberance of BVO-NRs will split into two evident peaks indexed as (200) and (002) and the intensity is strengthened as well implying the improved crystallinity of HT-BVO-NRs.

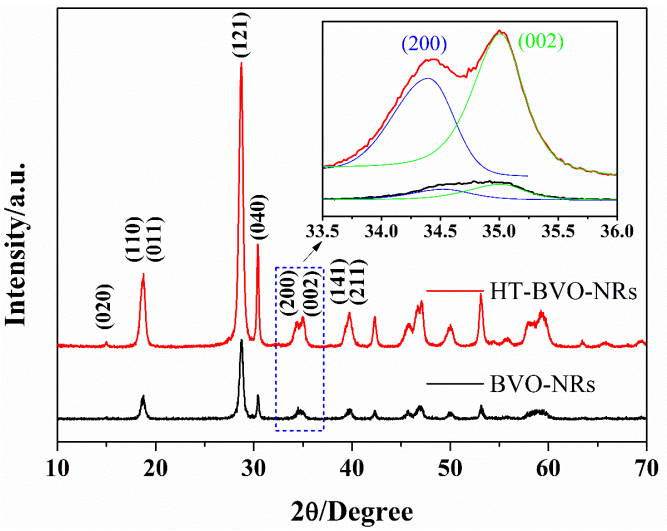

Fig. 2 Indexed XRD patterns of BVO-NRs and HT-BVO-NRs. The magnified peaks of (200) and (002) planes of BVO-NRs and HT-BVO-NRs in the range of 33.5 °to 36 °are shown in the inset.

X-ray photoelectron spectroscopy (XPS) is conducted to identify the chemical states of the *m*-$BiVO_4$ surface before and after heat treatment. As shown in Fig. S4, the XPS full-spectra of BVO-NRs and HT-BVO-NRs are essentially the same. Apart from the V, Bi and O peaks originated from *m*-$BiVO_4$, C 1s signal at 284.8 eV, which is believed to be mainly introduced during the sample preparation process, is also observed and used as binding energy (BE) reference, as displayed in Fig. 3(a). In addition, the broader C 1s peak for BVO-NRs and the small peak at 289 eV for HT-BVO-NRs, which are discussed in detail in the supplementary material (Fig. S4), should be resulted from sodium oleate used in the hydrothermal process and its oxidation products. Fig. 3(b) shows the V 2p signals of BVO-NRs and HT-BVO-NRs. The peaks of the XPS signals of the V $2p_{3/2}$ and V $2p_{1/2}$ are found at 516.5 eV and 524.3 eV, respectively, which coincide with the reported values for *m*-$BiVO_4$. [36] However, the asymmetric V $2p_{3/2}$ peak of BVO-NRs also indicates the existence of V^{4+} species and the ratio of V^{5+}: V^{4+} is estimated to be 69:31 using the Gaussian-Lorentzian (GL) fitting method. Hence, there should be a mass of oxygen vacancies that induced by V^{4+} on the surface of the pristine BVO-NRs, too. It is worth noting that, for an *m*-$BiVO_4$ nanorod which is 15 nm to 20 nm in diameter, the volume fraction that can be analyzed by XPS is around 75% because the detecting depth of XPS for oxides is

about 5 nm, as shown in Fig. S5. [37] In other words, V^{4+} species is distributed throughout the nanorod, as well as the oxygen vacancies. Although the V $2p_{3/2}$ peak of HT-BVO-NRs seems to be symmetric, it's hard to say that the content of V^{4+} species is negligible in this sample as many reported Ti^{3+} self-doped TiO_2 with high concentration of Ti^{3+} ions also presents a symmetric Ti $2p_{3/2}$ peak. [38-41] Oxygen vacancies with positive charge on the surface tend to adsorb some negative charged species, such as OH^- and O^{2-} whose binding energies are around 531.5 eV, as shown in Fig. 3(c). [23] The ratio of adsorbed O (O_{ads}) and lattice O (O_{latt}) on the surface of the BVO-NRs, which is calculated to be 66:34 using GL fitting methods, could be greatly decreased to 34:65 for HT-BVO-NRs. But, nevertheless, the remaining O_{ads} in HT-BVO-NRs is considerable suggesting V^{4+} ions are only partially oxidized after heat treatment. The binding energies of Bi $4f_{7/2}$ and Bi $4f_{5/2}$ are ~159.0 eV and ~164.3 eV, respectively, which agree well with the values reported in previous studies, as shown in Fig. 3(d).[42] In comparison to BVO-NRs, a small shift of 0.2 eV to higher energy for Bi 4f peaks are found in HT-BVO-NRs. This phenomenon can be ascribed to the oxidation some V^{4+} ions and is explained at length in the supplementary material (Fig. S4). [23]

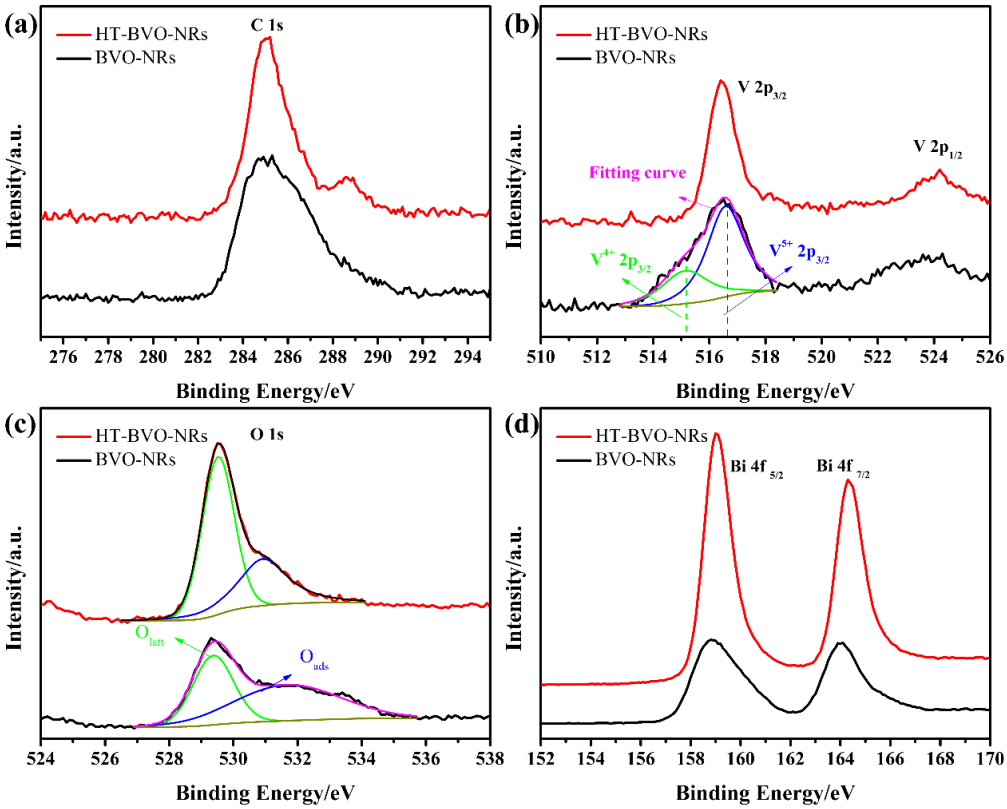

Fig.3 High-resolution XPS spectra of the (a) V 2p, (b) Bi 4f, (c) O1s and (d) C 1s of the pristine BVO-NRs and the HT-BVO-NRs. The curve fitting of the V 2p and O 1s spectra are also depicted.

In order to further identify the presence of V^{4+} ions in BVO-NRs and HT-BVO-NRs, EPR measurement was carried out at room temperature, as shown in Fig. 4. Theoretically, V^{5+} with $[Ar]3d^04s^0$ configuration will not show any signals in EPR spectrum, as well as Bi^{3+} ($[Xe]4f^{14}5d^86s^26p^0$) and O^{2-} ($1s^22s^22p^6$).[43] However, both BVO-NRs and HT-BVO-NRs give rise to broad signals at g=1.976 (3572.7 G), which is the typical g value for paramagnetic V^{4+}, indicating the presence of V^{4+} in these two samples.[44] Moreover, in comparison with BVO-NRs, the intensity of EPR signals for V^{4+} in HT-BVO-NRs is much weaker, suggesting a lower concentration of V^{4+}. The EPR results agree well with the conclusion derived from O 1s peaks in Fig. 3(c) verifying that the proportion of O_{ads} is capable of predicting the concentration of V^{4+} in similar cases. It is worth noting that the broad EPR signal for V^{4+} here is mainly caused by the strong spin-orbit coupling at room temperature. [38, 43, 44]

Sodium oleate with C=C could be served as not only chelating agent and but also reducing agent. [11, 12] As we all know, the hydrolysis of NH_4VO_3 and $Bi(NO_3)_3$ in water can generate a mass of H^+. It has been investigated that, in acid solutions, VO_4^{3+} mainly exist in the form of VO_2^+ whose standard electrode potential is as large as +1.0 V ($VO_2^+ + 2H^+ + e^- = VO^{2+} + H_2O$, $\varphi^\Theta = +1.0\,V$) and close to that of $Cr_2O_7^{2-}$ ($Cr_2O_7^{2-} + 14H^+ + 6e^- = 2Cr^{3+} + 7H_2O$, $\varphi^\Theta = +1.33\,V$) indicating its strong oxidability. [45] What's more, the oxidizing ability of VO_2^+ could be further enhanced under high temperature and high pressure conditions in the autoclave. Hence, self-doped $BiVO_4$ could be obtained after hydrothermal reaction in the presence of sodium oleate because V^{5+} can be reduced to V^{4+} species. A lot of efforts have been made to investigate the effect of dopants on the photocatalytic activities of m-$BiVO_4$. [46, 47] Although dopants in m-$BiVO_4$ could inhibit electron-hole recombination and increase the density of charge carriers in many cases, only a few of them achieved positive results because these dopants are likely to impede the charge transport at the same time by acting as scattering centers. Even in these cases that photocatalytic performances could be enhanced by doping, only appropriate amount of dopants (less than 10 at. %) were favorable which further demonstrated the important role of their scattering effect of charge carriers. [22, 48, 49] Therefore, the excess V^{4+} species

(around 31 at. %) which exists throughout the BVO-NRs will hinder the charge transport in BVO-NRs and subsequently recede its photocatalytic activity to some extent. Therefore, it is beneficial to reduce the content of V^{4+} and heat treatment as a quite convenient way is adopted.

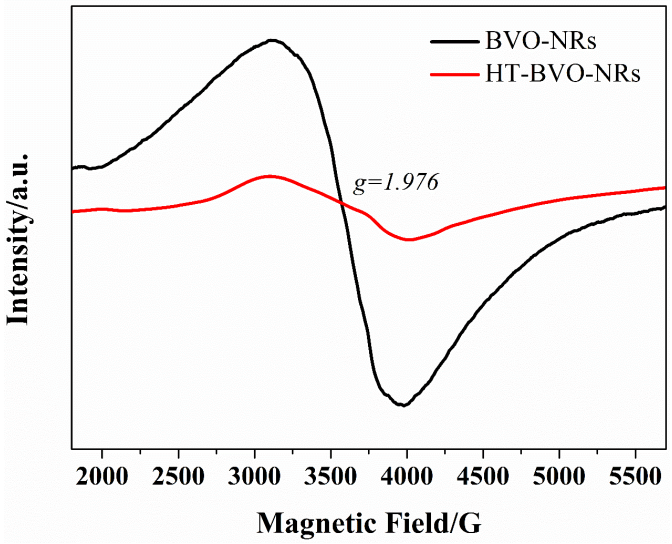

Fig. 4 Room temperature EPR spectra of BVO-NRs and HT-BVO-NRs.

The UV-Vis absorption spectra of the BVO-NRs and HT-BVO-NRs are shown in the inset of Fig. S6. It is found that the absorption edge of BVO-NRs shifts to a longer wavelength and the absorption in the wavelength range beyond 480 nm is enhanced after heat treatment. *m*-$BiVO_4$ is reported to be a direct band gap semiconductor and its band gap can be determined using Tauc's relation: $\alpha hv=A(hv-E_g)^{1/2}$ (where *h, v, A, E_g* and α stand for Planck's constant, light frequency, absorbance constant, band gap and absorption coefficient, respectively) by plotting $(\alpha hv)^2$ versus the photon energy *hv* near the absorption edge, as shown in Fig. S6. [50, 51] The band gaps for BVO-NRs and HT-BVO-NRs are estimated to be 2.55 eV and 2.57 eV, correspondingly.

Photocatalytic activities of BVO-NRs and HT-BVO-NRs are both evaluated by the degradation of Rh B under visible-light irradiation (λ>420 nm), as displayed in Fig. 5 and Fig. S7. For comparison, the degradation reactions in the presence of commercial Degussa P25 and without any photocatalyst are also conducted. It is found that the degradation of Rh B without catalysts is negligible and only 4% of Rh B is decomposed by P25 within 20 min under the same conditions. In comparison with traditional P25 catalyst, the BVO-NRs shows highly efficient photocatalytic activity and only 16 min is consumed to completely degrade Rh B in the aqueous solution. It is also worth noting that 61% of Rh B is adsorbed by the BVO-NRs before irradiation indicating an extremely strong adsorption capacity which is probably resulted from electrostatic attraction between the positive charged Rh B and adsorbed negative charged O^{2-} and OH^- species and the large specific surface area of BVO-NRs (28.2 m^2 g^{-1}).[23, 52, 53] More strikingly, the time that required to entirely decompose Rh B is reduced to as few as 9 min using HT-BVO-NRs under the same conditions even though its adsorption for Rh B is weakened greatly (23% of Rh B). The decrease on the adsorption effect should predominantly be ascribed to the removal of oxygen vacancies because the specific surface area of HT-BVO-NRs (27.8 m^2 g^{-1}) is basically the same with BVO-NRs (28.2 m^2 g^{-1}). For the purpose of judging whether the adsorbed Rh B is decomposed or not, the FTIR spectra are recorded for HT-BVO-NRs that collected before and after irradiation, respectively, as displayed in Fig. S8. Obvious characteristic peaks of Rh B are observed for the HT-BVO-NRs collected before photodegradation owing to its strong adsorption ability while all these peaks almost completely disappeared after irradiation implying the adsorbed Rh B is also oxidized. The kinetics of the photo-oxidation of Rh B is described as a pseudo-first-order reaction mode because of its relatively low concentration (10 mg L^{-1}). [54] The overall rate constant of reaction (*k*) could be derived from the regression curves of ln (C_0/C) *vs* irradiation time (*t*) for Rh B degradation, as shown in Fig. 6. The P25 catalyst shows an inappreciable *k* value of 0.0037 min^{-1} while the k value for BVO-NRs is as high as 0.141 min^{-1}, nearly 38 times to that of P25. More significantly, the k value is doubled for HT-BVO NR reaching 0.325 min^{-1}. As we all know, high stability is an essential feature for photocatalysts in practical applications. The stability of HT-BVO-NRs is tested by reusing the catalyst for five times, as shown in Fig. 7. The photocatalytic activity of HT-BVO-NRs is quite stable because no noticeable deactivation is observed after five consecutive cycles. In addition, apart from the well retained photocatalytic performance, the excellent adsorption of Rh B shows no decline as well which is consistent with the above mentioned FTIR results.

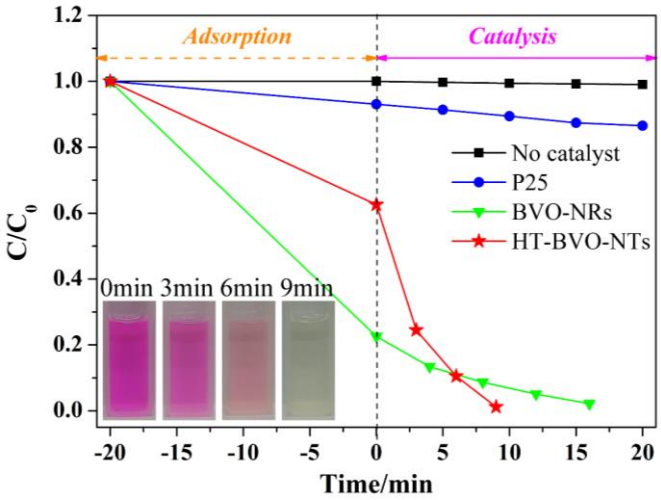

Fig. 5 Adsorption and photocatalytic degradation of Rh B in the presence of P25, BVO-NRs, HT-BVO-NRs and without catalyst.

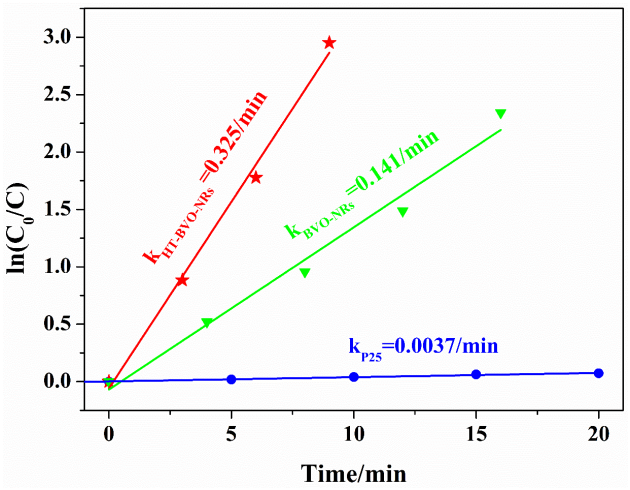

Fig. 6 ln (C_0/C) as a function of irradiation time (t) for Rh B degradation using P25, BVO-NRs and HT-BVO-NRs.

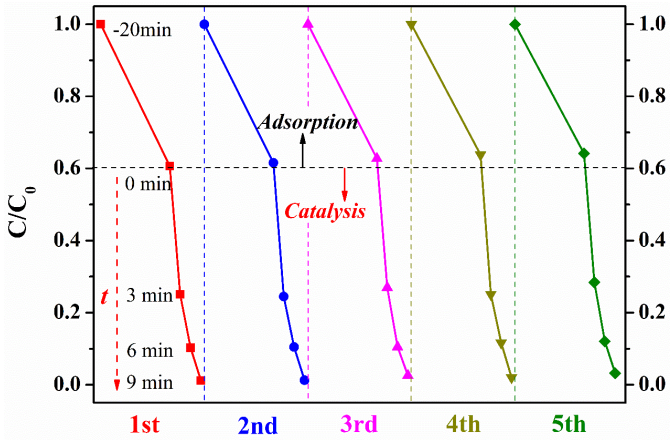

Fig. 7 Stability of the HT-BVO-NRs after consecutive cycling adsorption and photocatalytic degradation of Rh B.

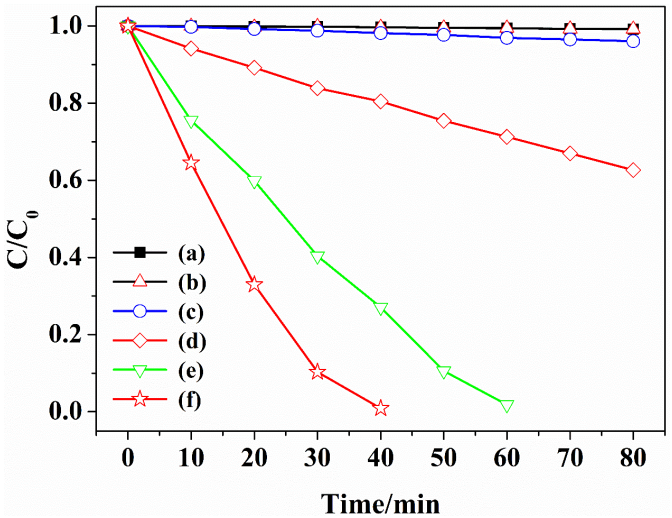

Fig. 8 Photocatalytic degradation of phenol with (a) H_2O_2 under visible light, (b) HT-BVO-NRs + 0.3 ml H_2O_2 in the dark, (c) Degussa P25 + 0.3 ml H_2O_2 under visible light, (d) HT-BVO-NRs under visible light, (e) BVO-NRs + 0.3 ml H_2O_2 under visible light and (f) HT-BVO-NRs + 0.3 ml H_2O_2 under visible light.

In view of the sensitization of the Rh B dye, phenol as a typical colorless and toxic contaminant was also chosen to evaluate the photocatalytic performance of BVO-NRs and HT-BVO-NRs. Fig. 8 shows the photodegradation efficiency of phenol under various conditions. H_2O_2 as an efficient electron scavenger which can enhance the separation of electron-hole pairs and facilitate photocatalytic efficiency has been frequently used in phenol photodegradation experiments owing to phenol is more obstinate compared with Rh B. [15] As shown in Fig. 8, no degradation of phenol is observed with only H_2O_2 under visible light or with HT-BVO-NRs in the presence of 0.3 ml H_2O_2 in the dark. The photodegradation of phenol with P25 in the presence of 0.3 ml H_2O_2 under visible light is also negligible and only *ca.* 3% phenol is degraded within 80 min. It has been demonstrated that pure $BiVO_4$ in the absence of H_2O_2 shows very poor photocatalytic activity for phenol under visible light irradiation.[15, 42, 55] Surprisingly, it is clearly observed that HT-BVO-NRs could degrade about 40% of phenol under visible light with in the absence of H_2O_2 within 80 min suggesting its highly efficient photocatalytic activity. The photodegradation performance for phenol of BVO-NRs and HT-BVO-NRs is also compared in the presence of 0.3 ml H_2O_2 and both of them exhibit extremely superior photocatalytic activity compared with many reported results. [42, 55] It takes about 60 min for BVO-NRs to remove all the phenol in the solution while HT-BVO-NRs is capable of decomposing the phenol entirely within only 40 min. The excellent photodegradation performance of BVO-NRs and HT-BVO-NRs for colorless phenol further confirm that the degradation of Rh B comes mainly from the photocatalytic process of $BiVO_4$ nanorods rather than the photosensitized one. In addition, phenol molecules are barely adsorbed by either BVO-NRs or HT-BVO-NRs owing to the absence of strong electrostatic attraction between negatively charged O^{2-} and OH^- species and neutral phenol molecules (Fig. S9).

It has been widely accepted that the crystallite dimension, crystal structure, morphology, crystallinity, specific surface area and concentration of dopants have a significant influence on the photocatalytic performance of one photocatalyst.[56, 57] The impressive photocatalytic activity of both BVO-NRs and HT-BVO-NRs over Rh B and phenol should be attributed to the large specific surface area, one dimensional morphology and unique growth habit. As introduced above, *m*-BiVO4 nanorods with diameters ranging from 15~20 nm possess an ultra large specific surface area (*ca.* 28 $m^2\ g^{-1}$) which could provide abundant active sites for photocatalytic reactions at one time and allow highly efficient photodegradation of Rh B and phenol. Apart from the large specific surface area, the unique growth habit and one dimensional morphology also contribute to the high photocatalytic performance of *m*-BiVO4 nanorods greatly. It has been manifested that electrons prefer to accumulate on (010) surfaces, namely the two ends of the *m*-$BiVO_4$ nanorod preferentially grown along [010] direction, which is advantageous for photo generated electron-hole separation.[19] The one dimensional morphology makes the distance for holes to diffuse to the surface of *m*-$BiVO_4$ nanorods (15-20 nm in diameter) very short which undoubtedly increases the survival probability of photo-excited holes. By comparing the photocatalytic performance of BVO-NRs and HT-BVO-NRs, one can see an enhanced photocatalytic activity is obtained for HT-BVO-NRs and this is of great importance. As discussed above, the presence of abundant oxygen vacancies induced by V^{4+} and the low crystallinity of the as-obtained BVO-NRs are detrimental to its photocatalytic activity by hindering the migration of charge carriers. That's probably why the photocatalytic activity is further improved after a low temperature heat treatment (230 ℃). It is also worth noting that heat treatment at higher temperatures (≥250 ℃) is undesirable because higher temperatures will result in severe agglomeration for BVO-NRs and subsequently diminish its specific surface area seriously, as shown in Fig. S10. Besides, in order to demonstrate that the conductivity of charge carriers is elevated after heat treatment, EIS measurements are performed for both BVO-NRs and HT-BVO-NRs film electrodes, as shown in Fig. 9. The deduced equivalent circuit for the anodes (inset of Fig. 9) is made up of a solution resistance (R_s), a charge transfer resistance (R_{ct}) in parallel to a constant phase element (CPE). [49] Smaller R_{ct} indicating better charge transport characteristics and its value can be obtained from the diameter of the arc. The fitted value of R_{ct} using ZView for BVO-NRs is as large as 30281 Ω, three times of the value for HT-BVO-NRs (9629 Ω). Thus, the improved charge transport characteristic in HT-BVO-NRs should be the

key factor that is responsible for the enhanced photocatalytic property.

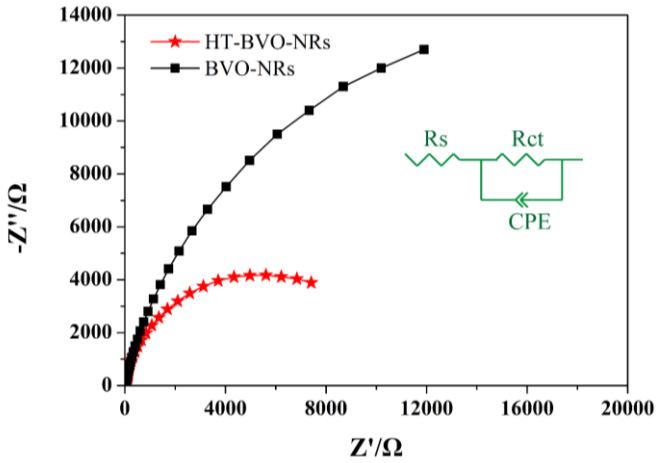

Fig. 9 Nyquist plots for BVO-NRs and HT-BVO-NRs electrodes measured in 0.1 M NaHCO3 aqueous solution (pH=7) at 0.7 V (vs. SCE) irradiated by a 350 W xenon lamp equipped with a 420 nm light cut-off filter from the uncoated side of the ITO glass (back side). The inset shows the equivalent circuit.

Conclusion

In summary, we successfully prepared self-doped *m*-$BiVO_4$ nanorods which were 15-20 nm in diameter and preferentially grown along [010] direction using a one-step low temperature hydrothermal method in the absence of toxic, expensive additives and strong acids. The as-prepared BVO-NRs showed extremely high photocatalytic activity which was primarily ascribed to its large specific surface area (28.2 $m^2 g^{-1}$), small size, and preferentially growth direction. Excellent adsorption ability of the BVO-NRs for Rh B, which was resulted from the abundant oxygen vacancies induced by V^{4+} species and the high specific surface area, was also observed. More importantly, the photocatalytic performance of the BVO-NRs was further improved to an unprecedented level simply by heating at 230 ℃ for 2 h, despite of the depressed adsorption ability. This distinct improvement was mainly owing to the modified charge transport characteristic brought about by the reduction of charge carrier scattering centers, including crystal imperfections caused by low crystallinity and V^{4+} species, after heat treatment. The HT-BVO-NRs also showed good stability in five consecutive cycling photodegradation tests. Our work could provide more insights into the influence of the crystallinity and the V^{4+} species on the photocatalytic activity of *m*-$BiVO_4$.

Acknowledgments

This work is supported by the Natural Science Foundation of China (No. 11474199 and 11074165). Instrumental Analysis Center of Shanghai Jiao Tong University is sincerely acknowledged for assisting relevant analyses.

Notes and references

Address: *State Key Laboratory of Metal Matrix Composites, School of Materials Science and Engineering, Shanghai Jiaotong University, Shanghai 200240, The People's Republic of China.*

† Electronic Supplementary Information (ESI) available: [details of any supplementary information available should be included here]. See DOI: 10.1039/b000000x/

1 H. Li, G. Liu, S. Chen, Q. Liu and W. Lu, *Physica E*, 2011, **43**, 1323-1328.
2 H. Kisch, *Angew. Chem. Int. Edit.*, 2013, **52**, 812-847.
3 S. U. Khan, M. Al-Shahry and W. B. Ingler, *Science*, 2002, **297**, 2243-2245.
4 Y.-S. Xu and W.-D. Zhang, *Dalton. T.*, 2013, **42**, 1094-1101.
5 M. Murdoch, G. Waterhouse, M. Nadeem, J. Metson, M. Keane, R. Howe, J. Llorca and H. Idriss, *Nat. Chem.*, 2011, **3**, 489-492.
6 H. G. Yang, C. H. Sun, S. Z. Qiao, J. Zou, G. Liu, S. C. Smith, H. M. Cheng and G. Q. Lu, *Nature*, 2008, **453**, 638-641.
7 M. Iqbal, *An introduction to solar radiation*, Academic Press, New York, 1983.
8 X. Chen, L. Liu, Y. Y. Peter and S. S. Mao, *Science*, 2011, **331**, 746-750.
9 A. Kudo, K. Ueda, H. Kato and I. Mikami, *Catal. Lett.*, 1998, **53**, 229-230.
10 Y. Park, K. J. McDonald and K. S. Choi, *Chem. Soc. Rev.*, 2013.
11 Y. Sun, B. Qu, Q. Liu, S. Gao, Z. Yan, W. Yan, B. Pan, S. Wei and Y. Xie, *Nanoscale*, 2012, **4**, 3761-3767.
12 Y. Sun, Y. Xie, C. Wu, S. Zhang and S. Jiang, *Nano Research*, 2010, **3**, 620-631.
13 S. Dong, J. Feng, Y. Li, L. Hu, M. Liu, Y. Wang, Y. Pi, J. Sun and J. Sun, *Appl. Catal. B-Environ.*, 2014, **152**, 413-424.
14 W. Wang, X. Huang, S. Wu, Y. Zhou, L. Wang, H. Shi, Y. Liang and B. Zou, *Appl. Catal. B-Environ.*, 2013, **134**, 293-301.
15 M. Shang, W. Wang, S. Sun, J. Ren, L. Zhou and L. Zhang, *J. Phys. Chem. C*, 2009, **113**, 20228-20233.
16 S. J. Hong, S. Lee, J. S. Jang and J. S. Lee, *Energ. Environ. Sci.*, 2011, **4**, 1781-1787.
17 W. Yao, H. Iwai and J. Ye, *Dalton. T.*, 2008, 1426-1430.
18 J. Pan, G. Liu, G. Q. M. Lu and H. M. Cheng, *Angew. Chem. Int. Edit.*, 2011, **50**, 2133-2137.
19 R. Li, F. Zhang, D. Wang, J. Yang, M. Li, J. Zhu, X. Zhou, H. Han and C. Li, *Nat. Commun.*, 2013, **4**, 1432.
20 G. Xi and J. Ye, *Chem. Commun.*, 2010, **46**, 1893-1895.
21 G. Silversmit, D. Depla, H. Poelman, G. B. Marin and R. De Gryse, *J. Electron. Spectrosc.*, 2004, **135**, 167-175.
22 G. Wang, Y. Ling, X. Lu, F. Qian, Y. Tong, J. Z. Zhang, V. Lordi, C. Rocha Leao and Y. Li, *J. Phys. Chem. C*, 2013, **117**, 10957-10964.
23 D.-D. Qin, T. Wang, Y.-M. Song and C.-L. Tao, *Dalton. T.*, 2014, **43**, 7691-7694.
24 J. Leyton, P. Drury and M. Crawford, *Brit. J. Nutr.*, 1987, **57**, 383-393.
25 J. Yu, Q. Xiang and M. Zhou, *Appl. Catal. B-Environ.*, 2009, **90**, 595-602.
26 O. Akhavan, *ACS Nano*, 2010, **4**, 4174-4180.
27 Y. Sun, C. Wu, R. Long, Y. Cui, S. Zhang and Y. Xie, *Chem. Commun.*, 2009, 4542-4544.
28 F. Dong, Q. Wu, J. Ma and Y. Chen, *Phys. Status Solidi A*, 2009, **206**, 59-63.
29 D. Wang, R. Li, J. Zhu, J. Shi, J. Han, X. Zong and C. Li, *J. Phys. Chem. C*, 2012, **116**, 5082-5089.
30 L. Hou, L. Yang, J. Li, J. Tan and C. Yuan, *J. Anal. Meth. Chem.*, 2012, **2012**.

31 A. A. Kelly and K. M. Knowles, *Crystallography and crystal defects*, John Wiley & Sons, West Sussex, 2012.
32 P. L. Gai-Boyes, *Catal. Rev.*, 1992, **34**, 1-54.
33 H. Kato, K. Asakura and A. Kudo, *J. Am. Chem. Soc.*, 2003, **125**, 3082-3089.
34 W. Zhou, F. Sun, K. Pan, G. Tian, B. Jiang, Z. Ren, C. Tian and H. Fu, *Adv. Funct. Mater.*, 2011, **21**, 1922-1930.
35 J. B. Joo, Q. Zhang, M. Dahl, I. Lee, J. Goebl, F. Zaera and Y. Yin, *Energ. Environ. Sci.*, 2012, **5**, 6321-6327.
36 C. Yin, S. Zhu, Z. Chen, W. Zhang, J. Gu and D. Zhang, *J. Mater. Chem. A*, 2013.
37 S. Hüfner, *Photoelectron spectroscopy: principles and applications*, Springer-Verlag, New York, 2003.
38 J. Huo, Y. Hu, H. Jiang and C. Li, *Nanoscale*, 2014, **6**, 9078-9084.
39 S. Hoang, S. P. Berglund, N. T. Hahn, A. J. Bard and C. B. Mullins, *Journal of the American Chemical Society*, 2012, **134**, 3659-3662.
40 X. Jiang, Y. Zhang, J. Jiang, Y. Rong, Y. Wang, Y. Wu and C. Pan, *The Journal of Physical Chemistry C*, 2012, **116**, 22619-22624.
41 M. Liu, X. Qiu, M. Miyauchi and K. Hashimoto, *Chemistry of Materials*, 2011, **23**, 5282-5286.
42 Y. Liu, H. Dai, J. Deng, L. Zhang and C. T. Au, *Nanoscale*, 2012, **4**, 2317-2325.
43 N. M. Atherton, M. Davies and B. Gilbert, *Electron spin resonance*, Royal Society of Chemistry, Cambridge, 1996.
44 S. Gupta, N. Khanijo and A. Mansingh, *Journal of non-crystalline solids*, 1995, **181**, 58-63.
45 F. A. Cotton, G. Wilkinson, C. A. Murillo, M. Bochmann and R. Grimes, *Advanced inorganic chemistry*, John Wiley & Sons, New York, 1999.
46 H. Ye, J. Lee, J. S. Jang and A. J. Bard, *J. Phys. Chem. C*, 2010, **114**, 13322-13328.
47 W. Luo, Z. Yang, Z. Li, J. Zhang, J. Liu, Z. Zhao, Z. Wang, S. Yan, T. Yu and Z. Zou, *Energ. Environ. Sci.*, 2011, **4**, 4046-4051.
48 H. S. Park, K. E. Kweon, H. Ye, E. Paek, G. S. Hwang and A. J. Bard, *J. Phys. Chem. C*, 2011, **115**, 17870-17879.
49 W. Jo, J.-W. Jang, K.-j. Kong, H. Kang, J. Kim, H. Jun, K. Parmar and J. Lee, *Angew. Chem. Int. Edit.*, 2012, **51**, 3147-3151.
50 J. Tauc, R. Grigorovici and A. Vancu, *Phys. Status Solidi B*, 1966, **15**, 627-637.
51 C. Li, P. Zhang, R. Lv, J. Lu, T. Wang, S. Wang, H. Wang and J. Gong, *Small*, 2013, **9**, 3951-3956.
52 E. McCafferty and J. Wightman, *Surface and Interface Analysis*, 1998, **26**, 549-564.
53 W. Dong, C. W. Lee, X. Lu, Y. Sun, W. Hua, G. Zhuang, S. Zhang, J. Chen, H. Hou and D. Zhao, *Applied Catalysis B: Environmental*, 2010, **95**, 197-207.
54 W. Yao, B. Zhang, C. Huang, C. Ma, X. Song and Q. Xu, *J. Mater. Chem.*, 2012, **22**, 4050-4055.
55 H. Jiang, H. Dai, X. Meng, K. Ji, L. Zhang and J. Deng, *Applied Catalysis B: Environmental*, 2011, **105**, 326-334.
56 J. Yu and A. Kudo, *Advanced Functional Materials*, 2006, **16**, 2163-2169.
57 J. S. Valente, F. Tzompantzi, J. Prince, J. G. Cortez and R. Gomez, *Applied Catalysis B: Environmental*, 2009, **90**, 330-338.

